



A measurement of the cosmic-ray muon flux with a module of the NESTOR neutrino telescope

The NESTOR Collaboration

G. Aggouras^j, E.G. Anassontzis^{a,*}, A.E. Ball^d, G. Bourlis^f, W. Chinowsky^h,
E. Fahrún^g, G. Grammatikakis^e, C. Green^g, P. Grieder^b, P. Katrivanosⁱ,
P. Koske^g, A. Leisos^{j,f}, E. Markopoulos^j, P. Minkowsky^c, D. Nygren^h,
K. Papageorgiou^j, G. Przybylski^h, L.K. Resvanis^{a,j}, I. Siotisⁱ, J. Sopher^h,
A. Staveris-Polikalas^j, V. Tsagli^j, A. Tsirigotis^{j,f}, V.A. Zhukov^k

^a *University of Athens, Physics Department, Panepistimioupolis, 15771 Ilissia Athens, Greece*

^b *University of Bern, Physikalisches Institut, Switzerland*

^c *University of Bern, Institute for Theoretical Physics, Switzerland*

^d *CERN (European Organization for Nuclear Research), Geneva, Switzerland*

^e *University of Crete, Physics Department, Greece*

^f *Hellenic Open University, School of Science and Technology, Patra, Greece*

^g *University of Kiel, Institute of Experimental and Applied Physics, Germany*

^h *Lawrence Berkeley National Laboratory, Berkeley, CA, USA*

ⁱ *NCSR "Demokritos", Athens, Greece*

^j *NESTOR Institute for Deep Sea Research, Technology and Neutrino Astroparticle Physics, Pylos, Greece*

^k *Institute for Nuclear Research, Russian Academy of Sciences, Moscow, Russia*

Received 5 January 2005; accepted 10 February 2005

Available online 11 March 2005

Abstract

A module of the NESTOR underwater neutrino telescope was deployed at a depth of 3800 m in order to test the overall detector performance and particularly that of the data acquisition systems. A prolonged period of running under stable operating conditions made it possible to measure the cosmic ray muon flux, $I_0 \cdot \cos^2(\theta)$, as a function of the zenith angle θ . Measured values of index α and the vertical intensity I_0

* Corresponding author. Tel./fax: +30 210 7276948.

E-mail address: eanason@cc.uoa.gr (E.G. Anassontzis).

$$\alpha = 4.7 \pm 0.5(\text{stat}) \pm 0.2(\text{syst})$$

$$I_0 = 9.0 \times 10^{-9} \pm 0.7 \times 10^{-9}(\text{stat}) \pm 0.4 \times 10^{-9}(\text{syst}) \text{ cm}^{-2} \text{ s}^{-1} \text{ sr}^{-1}$$

are in good agreement with previous measurements and phenomenological predictions.

© 2005 Elsevier B.V. All rights reserved.

PACS: 95.55.Vj; 29.40.Ka; 13.15.+g

Keywords: Neutrino; Telescope; Deep-sea; NESTOR; Muon flux

1. Introduction

Measurements of the atmospheric muon flux provide information [1,2] on the energy spectrum and composition of primary cosmic rays as well as the nuclear-cascade mechanisms for the production and propagation of high energy nucleons, pions, kaons and charmed mesons in the atmosphere.

In addition to the direct measurements at sea level [3–5], the measurement at varying depths underground or underwater/ice allow an exploration of the high energy component of the atmospheric muon spectrum. Underwater measurements are particularly interesting as they have lower systematic errors because of the large detection volume, its uniformity and the known composition of the matter overburden.

Presented here are the results of a first stage experiment of the NESTOR (Neutrino Extended Submarine Telescope with Oceanographic Research) project, the principal objective of which was to test the data acquisition systems under operational conditions. The ultimate aim of NESTOR is to build a high resolution, large effective area, deep sea neutrino telescope [6,7] having several “floors” or hexagonal “stars” with Ti arms that support 15 in. photomultiplier tubes (PMT) at their extremities: the PMTs are mounted in pairs inside Benthos glass housings [8] looking upwards and downwards at a diameter of 32 m. The NESTOR collaboration has located an 8 km × 9 km horizontal plateau at a mean depth of 4000 m close to the deepest part of the Mediterranean, southwest of the Peloponnesse. Extensive studies of the environmental properties [9–11] show that the

water is remarkably clear, having a light transmission length of 55 m at a wavelength of 460 nm, and the underwater currents are minimal [12].

The test detector that was deployed in March 2003 [13–15] consisted of a single Ti hexagonal floor of 12 m diameter. The electronics [16,17] that provide the signal sensing, triggering, digitization and data transmission to the shore, as well as controlling and monitoring the PMTs, were housed inside a titanium sphere, about 1 m in diameter, located at the center of the floor. This detector floor was positioned at 80 m above the sea bottom station (pyramid) that houses the anchor, an environmental instrument package and the junction box for the electro-optical cable that connects the assembly to the shore laboratory.

The atmospheric muon vertical intensity and the muon zenith angle distribution have been measured at a depth of 3800 m. The deployed detector has been operated continuously for more than a month and over 5 million events have been accumulated with different trigger modes, coincidence levels and PMT thresholds. Some 40% of these events are reported on here: the selected events have been accumulated under constant conditions during 7 days of running time with a 4-fold or higher coincidence trigger and 30 mV threshold¹ for each PMT, at a trigger rate of ~3.8 Hz. The readout and DAQ chain was operated continuously with essentially zero dead time and the monitored experimental parameters (environmental and operational) remained stable throughout.

¹ The mean PMT pulse height corresponding to one photoelectron was 120 mV.

A detailed description of the operation and performance of this prototype detector has been published elsewhere [15]. This work concentrates on the processing of the accumulated data in order to reconstruct muon tracks and on the estimation of the differential atmospheric muon flux at the detector depth, integrated over energy. It contains results from several studies to evaluate the capability of the detector to detect muons and correctly reconstruct their trajectories. This is a critical test for the NESTOR project, since the neutrino detection and direction depends on the reconstructed (mainly upward-going) muon trajectories.

2. Muon trajectory reconstruction

Only a small fraction (2%) of the events, selected with a 4-fold or higher coincidence level trigger and a 30 mV PMT threshold, had six or more PMT pulses inside a time window² of 60 ns. These events were used to reconstruct muon tracks employing first the information on the arrival time and then the amplitude of the digitized pulses.

In parallel, a simulation package [15] has been developed to produce a Monte Carlo event sample corresponding to the simulated detector response to atmospheric muons arriving at the detector depth. Using the energy and angular distributions taken from the Okada parameterization [18], a large number of muons (2.26×10^7) were generated within a 100 m radius circle at 100 m vertically above the detector plane (roughly two transmission lengths). These simulated muons were propagated through the water, taking into account the energy loss mechanisms³ (ionization and atomic excitations, pair production, bremsstrahlung, nuclear interactions), the secondary particle production (e.g. electromagnetic shower development) and multiple scattering. After this, a detailed simulation of the Cherenkov light detection, K^{40} background contribution, trigger selection and

PMT waveform digitization has been made. The Monte Carlo simulated data are packaged with the same protocol as the experimental data and then can be analysed in exactly the same way as the real data.

2.1. Track reconstruction

In the first stage of the track reconstruction, the algorithm makes use of all the PMT pulses lying inside the coincidence window (hits). However, when a PMT waveform consists of multiple hits, all within the coincidence window, only the higher amplitude pulse is considered. The other hits on this PMT are used in cases where the reconstruction procedure does not converge or when the selected hit is rejected during the second reconstruction stage.

The arrival times of the selected hits are used in a χ^2 minimization in order to estimate the track parameters and evaluate the error matrix of the estimates. The χ^2 estimator is defined (see also Fig. 1) as

$$\chi^2 = \sum_{i=1}^{N_{\text{hit}}} \left(\frac{t_i^{\text{exp}} - t_i^{\text{data}}}{\sigma_i^{\text{data}}} \right)^2 \quad (1)$$

where N_{hit} is the number of the hits used for the track reconstruction, $t_i^{\text{exp}} \equiv t_i^{\text{exp}}(\theta, \varphi, V_x, V_y, V_z)$ is

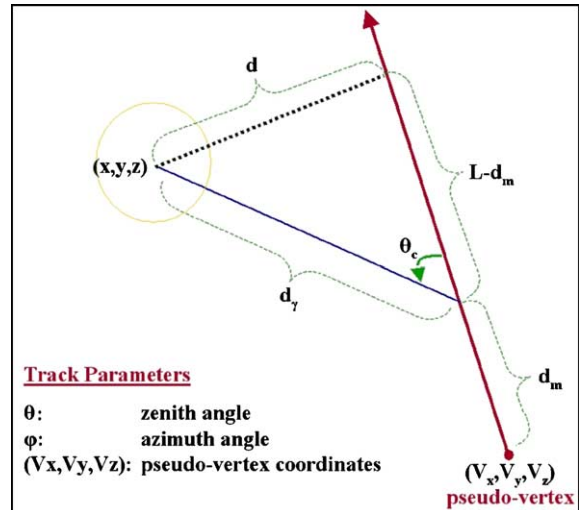


Fig. 1. Geometrical representation of the transmission of Cherenkov light to a PMT.

² In the following, this time window will be referred as “coincidence window”.

³ All references to the energy and zenith angle of the muons are considered to be at the detector depth.

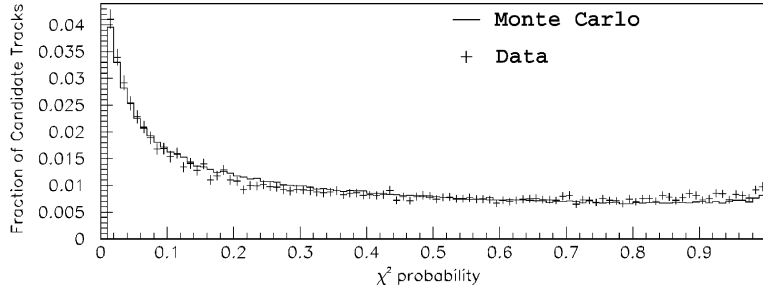


Fig. 2. The χ^2 probability distribution of candidate tracks (crosses) in comparison to the Monte Carlo sample (solid line), at the end of the first reconstruction stage.

the expected arrival time⁴ of the i th hit, assuming that the pulse is the PMT response to the Cherenkov light produced by a muon track with zenith angle θ , azimuthal angle φ and pseudovertex⁵ coordinates $\{V_x, V_y, V_z\}$, t_i^{data} is the measured arrival time of the i th hit, σ_i^{data} is the resolution in measuring the arrival time of the i th hit. This has been measured for each PMT as a function of the pulse amplitude, both in the laboratory and in the deep sea [8,15]. The χ^2 minimization can often converge to multiple solutions, each corresponding to a candidate track.

Fig. 2 presents the χ^2 probability distribution of the candidate tracks from the data sample compared with the χ^2 probability distribution from a sample of Monte Carlo events, treated in the same way as the real data. In both data and Monte Carlo there is an excess of events at lower probabilities due to false track candidates.

⁴ The t^{exp} is evaluated by means of the geometrical elements shown in Fig. 1, as

$$t^{\text{exp}} = \frac{d_m}{c} + \frac{d_i}{(c/n)} = \frac{(L + d \cdot \tan \theta_c)}{c},$$

$$L = \cos \varphi \cdot \sin \theta \cdot (x - V_x) + \sin \varphi \cdot \sin \theta \cdot (y - V_y) + \cos \theta \cdot (z - V_z),$$

$$d = \{[(x - V_x) - L \cdot \cos \varphi \cdot \sin \theta]^2 + [(y - V_y) - L \cdot \sin \varphi \cdot \sin \theta]^2 + [(z - V_z) - L \cdot \cos \theta]^2\}^{1/2}$$

where $\{x, y, z\}$ are the coordinates of the PMT centre.

⁵ This is a point on the muon track corresponding to the start of the experimental time window.

The second reconstruction stage is an iterative attempt to improve the tracking resolution for each candidate found. The algorithm rejects the hit with the largest contribution to the χ^2 value and tests if this improves the χ^2 probability. Also in this stage, cases where multiple hits on a PMT have been recorded within the coincidence window, the hits with lower pulse height can be considered.

2.2. Track selection

Only those candidate tracks with a χ^2 probability greater than 0.1 are retained for further analysis. For each track candidate, the expected quantity of Cherenkov light reaching each of the PMT's in the detector can be compared to the measured pulse heights observed. Criteria can thus be established to further refine the trajectory selection.

A significant fraction of the events give more than one possible track solution from the pulse arrival time analysis alone. This is due to an inherent geometrical degeneracy (mirror solution), because there is symmetry between the Cherenkov light cones emitted from tracks that form an angle of twice the Cherenkov angle. This ambiguity can be resolved by examining the light intensity distribution on the PMTs.

To quantify this light distribution, a photon-likelihood, L_{ph} , is defined as

$$L_{\text{ph}} = \prod_{i=1}^{N_{\text{hit}}} P_i(V_{\text{data}}; \mu_{\text{exp}}) \quad (2)$$

where $P_i(V_{\text{data}}; \mu_{\text{exp}})$ is the probability that the pulse height of the i th hit is V_{data} when the expected mean number of photoelectrons emitted from the photocathode due to Cherenkov light, is μ_{exp} .

The expected mean number of photoelectrons, μ_{exp} , is calculated, taking into account the candidate track parameters and the PMT positions, the mean number of Cherenkov photons produced per unit track length, the PMT geometric cross section, the light absorption from the water and other materials, the PMT collection and quantum efficiency. The probability $P_i(V_{\text{data}}; \mu_{\text{exp}})$ is then estimated as the convolution of the Poissonian probability function, of mean value μ_{exp} , for the emission of n photoelectrons from the photocathode with the probability density function $R_i(V_{\text{data}}; n)$. This function, $R_i(V_{\text{data}}; n)$, expresses the probability of the i th hit to have a pulse height equal to V_{data} , assuming that the pulse is produced from the emission of n photoelectrons.

The function $R_i(V_{\text{data}}; n)$ is the pulse height distribution (normalized to unity), which corresponds to n photoelectrons. It has been evaluated for each of the PMTs by the convolution of n one-photoelectron pulse height distributions.⁶

Consequently the probability function $P_i(V_{\text{data}}; \mu_{\text{exp}})$ is expressed as

$$P_i(V_{\text{data}}; \mu_{\text{exp}}) = \sum_{n=1}^{\infty} \frac{(\mu_{\text{exp}})^n e^{-\mu_{\text{exp}}}}{n!} R_i(V_{\text{data}}; n) \quad (3)$$

Fig. 3 plots the distribution of the values of the negative logarithm of the photon-likelihood ($-\ln L_{\text{ch}}$) for candidate tracks that survive the second reconstruction stage, compared with the Monte Carlo estimation. It is seen later that a rejection of candidate tracks with negative logarithms of the photon-likelihood greater than 16, cleans the sample from mirror solutions. For the remaining multiple track candidates in an event, a track is selected if the χ^2 probability exceeds the χ^2 probability of the other candidate(s) by more than 0.1 or else has a lower $-\ln L_{\text{ch}}$ value.

⁶ The one-photoelectron pulse height distribution of each PMT has been measured in the laboratory, before the detector deployment, and it has been verified with the calibration data collected in the sea [15].

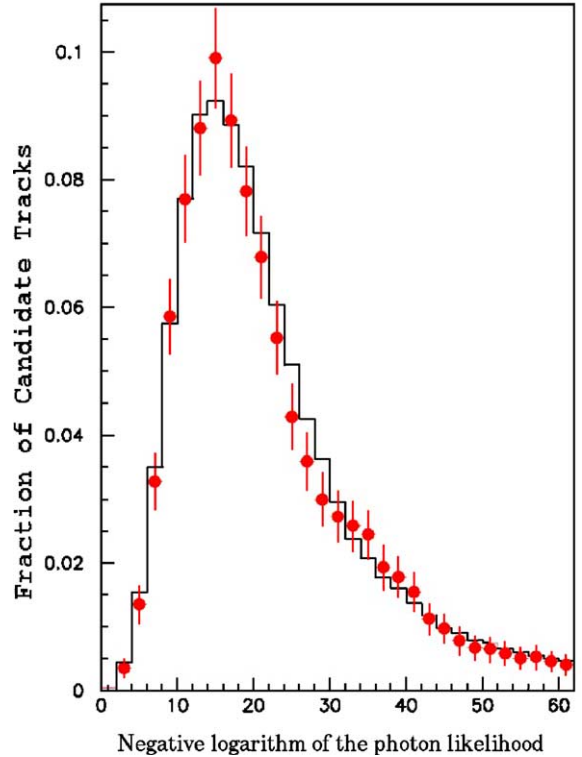


Fig. 3. The negative logarithm of the photon-likelihood for data (solid points) and Monte Carlo (histogram) candidate tracks surviving the second reconstruction stage.

Further Monte Carlo studies indicate that other selection criteria using the total number of photoelectrons carried by a track candidate⁷ and the impact parameter⁸ can reject badly reconstructed tracks. The number of photoelectrons per track and the impact parameter distributions for the data and Monte Carlo event samples are shown in Fig. 4. By selecting tracks with more than $4 \cdot N_{\text{hit}}$ photoelectrons the discrimination power of the photon-likelihood criterion is increased. In addition, by requiring the impact parameter of the reconstructed track to exceed the detector radius of 6 m, cases that cannot be

⁷ This is the sum of the pulse height of the hits (in units of the mean value of the one-photoelectron pulse height distribution) used in the fit.

⁸ This is the perpendicular distance of the reconstructed track from the center of the Ti-floor.

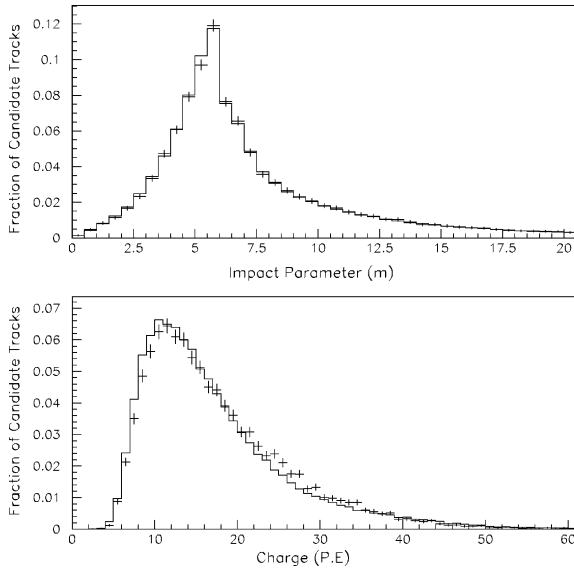


Fig. 4. Distributions of the impact parameter (above) and the total number of photoelectrons per track (below). The crosses represent the data, whilst the histograms show the Monte Carlo prediction for candidate tracks surviving the second reconstruction stage.

resolved correctly because of the small lever arm of the test detector are excluded.⁹

A total of 745 reconstructed muon tracks have been selected. The zenith angle distribution of the selected tracks is presented in Fig. 5 and compared with the Monte Carlo prediction for atmospheric muons following the parameterization of [18]. As has been shown in [15], the data are in a very good agreement with this phenomenological prediction. Note however that both the data and Monte Carlo distributions contain events with zenith angles greater than 90° , most probably due to resolution effects.

The estimated error of the zenith angle reconstruction is in good agreement with the Monte Carlo prediction as shown in Fig. 6. In both data and Monte Carlo samples, the estimated errors are peaked at a value of 8.5° with an average value of 11° .

In order to check that the track reconstruction algorithm gives consistent error estimations, the

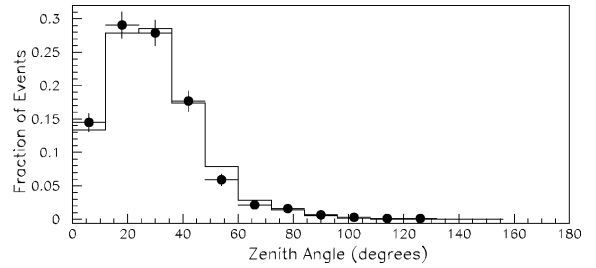


Fig. 5. The zenith angle distribution of the reconstructed tracks (solid points) in comparison with the Monte Carlo prediction (histogram).

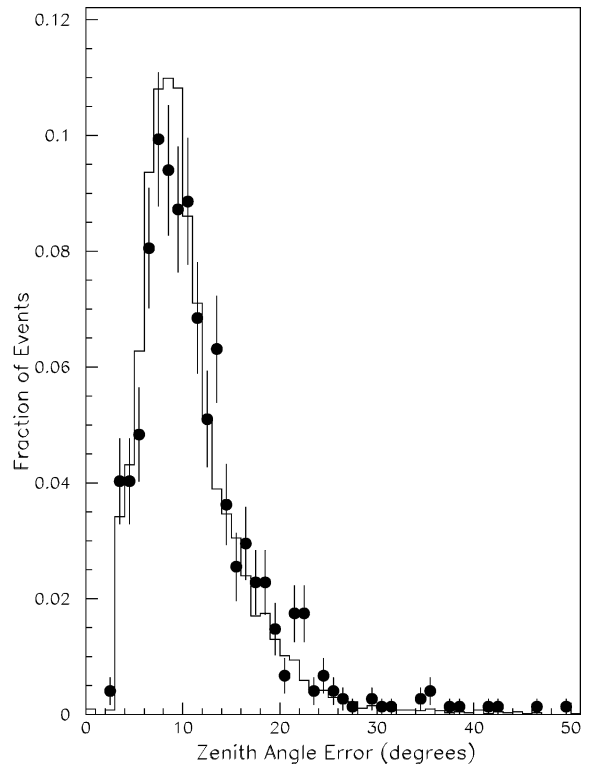


Fig. 6. Distribution of the estimated errors of the reconstructed zenith angles. The solid points and the histogram correspond to the data and Monte Carlo tracks respectively.

pull distribution for the reconstructed zenith angle was generated using the Monte Carlo event sample. The pull distribution is the deviation of the reconstructed zenith angle from its true value divided by the estimated error. Fig. 7 shows that the pull distribution exhibits Gaussian shape with

⁹ See Section 5 for a study of the systematic errors due to these selection criteria.

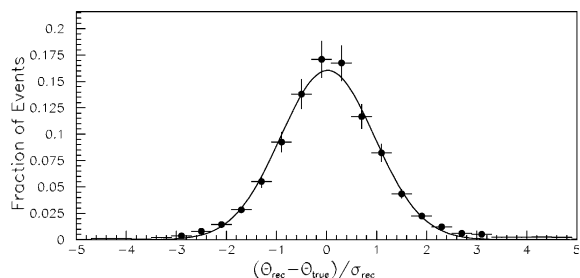


Fig. 7. The pull distribution of the reconstructed zenith angles of Monte Carlo produced tracks.

a mean value and sigma consistent with zero and one respectively.

Using the Monte Carlo event sample, the ways in which the various selection criteria affect the res-

olution of the zenith angle estimation have been studied. It can be seen in Fig. 8 that these selection criteria, applied throughout the reconstruction stages, reject the majority of badly fitted track candidates, especially the ghost “mirror” tracks.

The distribution of the difference between the reconstructed and the “true” zenith angle for the selected Monte Carlo tracks (Fig. 8a) exhibits a central Gaussian peak of a sigma equal to 8.5° , in a very good agreement with the most probable value of the error found in the data (see Fig. 6).

However, long tails remain, mainly due to the residual mirror solutions and, even after the application of the selection criteria, the average resolution is reduced to 12° : this is completely consistent

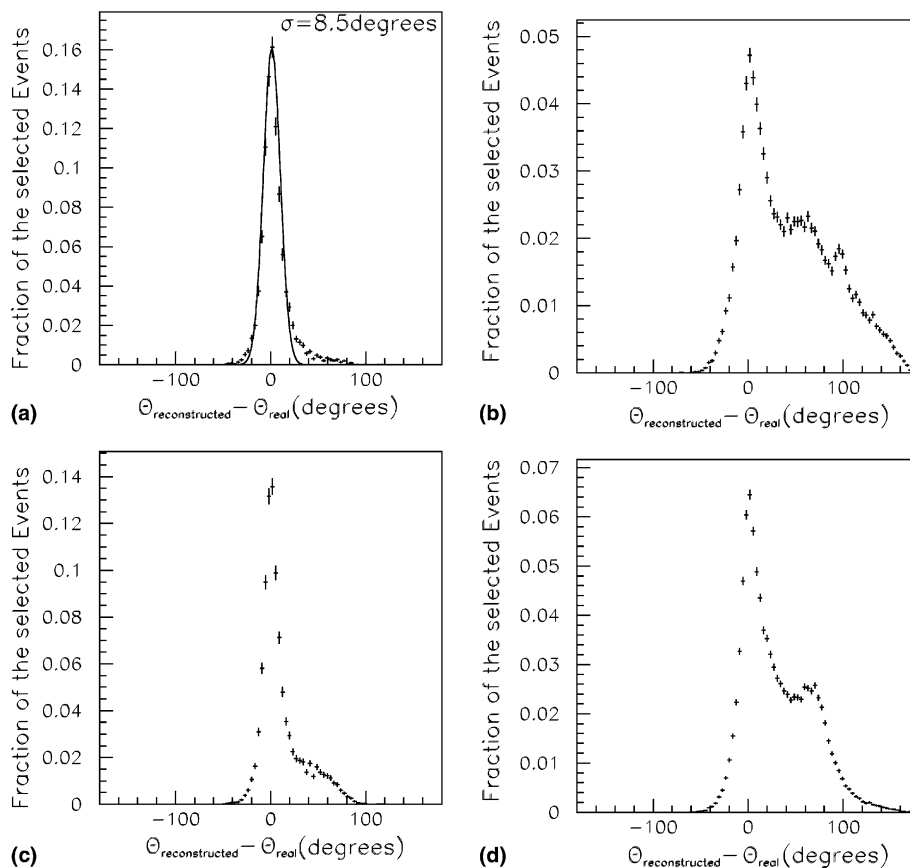


Fig. 8. Demonstration of the effect of the selection criteria on the resolution in reconstructing the zenith angle from the Monte Carlo event sample: (a) the resolution distribution of the selected track sample; (b) the resolution distribution without the photon-likelihood selection criteria; (c) the resolution distribution without the impact parameter selection criteria; (d) the resolution distribution without the selection criteria on the total number of photoelectrons per track.

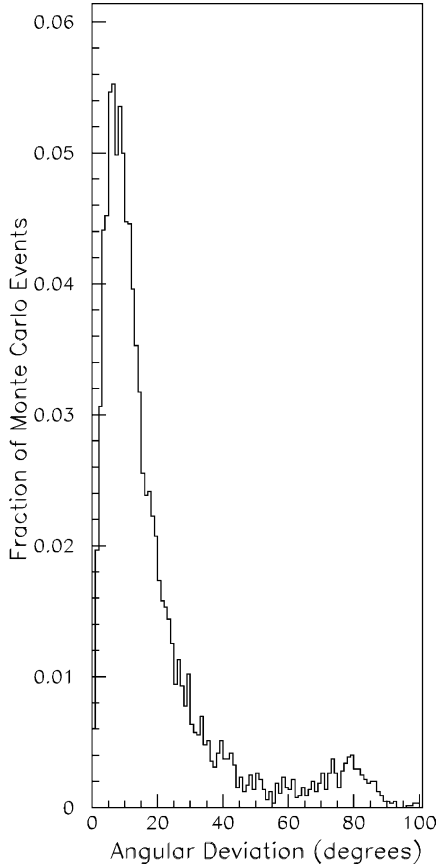


Fig. 9. The three-dimensional angular deviation of Monte Carlo tracks from their true direction.

with the average reconstructed error found in the data set.

Finally, Fig. 9 presents the three-dimensional angular deviation of the reconstructed tracks from their true direction, quantified using the Monte Carlo event sample. After applying the track selection criteria described above, more than 90% of the reconstructed tracks exhibit a mean angular deviation of 14° , whilst the remaining events are concentrated at high values from mirror solutions.

3. Measurement of the differential atmospheric muon flux

In order to measure the flux of atmospheric muons at 3800 m.w.e. depth, the raw data zenith

angle distribution, shown in Fig. 5 has been used: this has been sorted into equal size bins. As any correction factors are functions of the muon track parameters, the detector simulation package was used to convolute the physical fluxes with the detector response, the reconstruction efficiency and resolution by means of a Monte Carlo integration.

The measured data zenith angle distribution is compared to Monte Carlo expectations by employing a binned extended likelihood approach.

Let d_i , $i = 1, 2, \dots, k$, be the number of reconstructed data tracks with zenith angles in the i th bin. Then $D = \sum_{i=1}^k d_i$ is the total number of reconstructed data tracks.

Let $m_i(\vec{\epsilon})$, $i = 1, 2, \dots, k$, be the number of reconstructed tracks produced by a Monte Carlo in the i th bin, having gone through the whole detector simulation and reconstruction chain. The vector $\vec{\epsilon} = \{\epsilon_1, \dots, \epsilon_r\}$ contains the parameters that define the physical muon flux distribution used to generate the Monte Carlo events. Then $M(\vec{\epsilon}) = \sum_{i=1}^k m_i(\vec{\epsilon})$ is the total number of available reconstructed Monte Carlo tracks produced with generation parameters $\vec{\epsilon}$.

Similarly, let $m_i^o(\vec{\epsilon})$ be the number of the generated tracks with parameters $\vec{\epsilon}$ and zenith angles in the i th bin, before any acceptance, selection and reconstruction cuts. $M^o(\vec{\epsilon}) = \sum_{i=1}^k m_i^o(\vec{\epsilon})$ is the total number of generated Monte Carlo events with generation parameters $\vec{\epsilon}$, inside a cylinder with a radius of 100 m.

In the following, it is assumed that the atmospheric muon flux depends on the energy of the muon, as described by the parameterization of [18] and that the energy integrated muon flux can be parameterized as

$$\frac{dN}{d\Omega \cdot dt \cdot dS} = I_0 \cos^2 \theta \quad (4)$$

where N is the number of atmospheric muons passing through a horizontal disk of area S at the detector depth¹⁰: the symbols Ω , t and θ stand for the solid angle, time and zenith angle respectively.

¹⁰ This is the base of the cylinder inside which the Monte Carlo tracks are generated.

Eq. (4) implies that the differential flux is uniform with respect to time, azimuth angle and distance from the detector and that I_0 represents the vertical flux.¹¹ It also implies that the only relevant parameter in generating Monte Carlo events is the index, α in Eq. (4), and consequently $\vec{\varepsilon} = \{\varepsilon_1\} = \{\alpha\}$ is a one-dimensional vector.

The probability of observing one event at the i th bin of zenith angle can be estimated by Monte Carlo events, which have been generated according to the model (4), as

$$P_i(\alpha) = \frac{m_i(\alpha)}{M(\alpha)} \quad (5)$$

where α is the exponent in Eq. (4).

Then the probability of observing d_1, d_2, \dots, d_k events in the 1st, 2nd, \dots , k th zenith angle bins is given by the following formula:

$$P(\alpha) = \frac{D!}{d_1! \cdot d_2! \cdot \dots \cdot d_k!} \prod_{i=1}^k (P_i(\alpha))^{d_i} \quad (6)$$

In order to avoid statistical correlations between the bins, the extended likelihood estimator is formed as

$$L = \frac{(\lambda \cdot M(\alpha))^D \cdot e^{-\lambda \cdot M(\alpha)}}{D!} \cdot P(\alpha) \\ = \prod_{i=1}^k \frac{(\lambda \cdot m_i(\alpha))^{d_i} \cdot e^{-\lambda \cdot m_i(\alpha)}}{d_i!} \quad (7)$$

by multiplying the multinomial probability of Eq. (6) with the Poissonian probability of observing D tracks with an expectation $\lambda \cdot M(\alpha)$.

The parameter λ is a normalization factor, which has to be estimated from the data. This factor carries all the available information for the evaluation of the vertical muon flux, I_0 , of Eq. (4). The parameters λ and α can be derived simultaneously by minimizing the negative logarithm of the extended likelihood.

In order to avoid the generation of several Monte Carlo event samples at different values of α , the re-weighting technique described in [19] has been employed.

Specifically, it has been found that the energy integrated angular distribution used to produce the available¹² Monte Carlo sample can be approximated to the following formula:

$$\frac{dN}{dt \cdot dS \cdot d\Omega} \approx N_0 \cdot e^{-\frac{3.0}{\cos\theta}} \quad (8)$$

where N_0 is an overall normalization factor.

The relative probability of producing a muon with a zenith angle θ by a generation model following Eq. (4), with respect to the generation probability of the same muon by the model of Eq. (8), is given by the ratio:

$$w(\theta; \alpha) = \frac{\cos^\alpha \theta \cdot \sin \theta}{\int_0^{\pi/2} \cos^\alpha \theta \cdot \sin \theta \cdot d\theta} \\ \frac{\sin \theta \cdot e^{-\frac{3.0}{\cos\theta}}}{\int_0^{\pi/2} \sin \theta \cdot e^{-\frac{3.0}{\cos\theta}} \cdot d\theta} \\ = (\alpha + 1) \cdot \cos^\alpha \theta \cdot e^{-\frac{3.0}{\cos\theta}} \cdot \int_0^{\pi/2} \sin \theta \\ \cdot e^{-\frac{3.0}{\cos\theta}} \cdot d\theta \quad (9)$$

Using the relative probability, $w(\theta; \alpha)$ to weigh each of the tracks of the Monte Carlo sample, the populations $m_i(\alpha)$ can be estimated, for any value of the parameter α , as the sum of the weights:

$$m_i(\alpha) = \sum_{j=1}^{n_i} w(\theta_j; \alpha) \quad (10)$$

where n_i is the number of the available Monte Carlo reconstructed tracks with zenith angles θ_j , $j = 1, \dots, n_i$, which belong to the i th bin.

In order to include statistical uncertainties in the evaluation of the populations $m_i(\alpha)$, the definition of the extended likelihood has been modified to

$$L = \prod_{i=1}^k \left[\int_{m_i(\alpha)-b}^{\infty} \frac{(\lambda \cdot x)^{d_i} \cdot e^{-\lambda x}}{d_i!} \cdot \frac{1}{\sqrt{2\pi} \cdot \sigma_i} \right. \\ \left. \cdot e^{-\frac{(m_i(\alpha)-x)^2}{2\sigma_i^2}} \cdot dx \right] \quad (11)$$

¹² After the full detector simulation and track reconstruction a sample of 8460 Monte Carlo muon tracks, out of the 2.26×10^7 muons generated as described in Section 2, remains.

¹¹ This is the differential flux for a zenith angle equal to zero.

where b should go to infinity¹³ and σ_i is the error on the $m_i(\alpha)$ evaluation, which is given by the following simple formula of independent contributions:

$$\sigma_i = \left[\sum_{j=1}^{n_i} w^2(\theta_j; \alpha) \right]^{1/2} \quad (12)$$

Finally, in order to estimate the vertical muon intensity directly from the fit, the parameter λ can be expressed in terms of the vertical intensity (I_0 of Eq. (4)), the total experimental active time ($T = 609,580$ s), the total number of generated Monte Carlo events ($M_0(\alpha)$), the value of the spectral index (α) and the area of the disc ($S = 3.14 \times 10^8$ cm²) on which the Monte Carlo events were generated. Integrating Eq. (4) and setting the number of muons passing through a disk to be equal to the ($\lambda \cdot M_0(\alpha)$), it can be shown that

$$\lambda = \frac{I_0 \cdot 2\pi \cdot T \cdot S}{M_0(\alpha) \cdot (\alpha + 1)} \quad (13)$$

The simultaneous maximization of Eq. (11) with respect to I_0 and α , has been made using the MINUIT package from the CERN program library [20].

The reconstructed zenith angle, fitted from the data sample using bins of equal probability, has values of

$$\alpha = 4.7 \pm 0.5$$

$$I_0 = 9.0 \times 10^{-9} \pm 0.7 \times 10^{-9} \text{ cm}^{-2} \text{ s}^{-1} \text{ sr}^{-1} \quad (14)$$

with a correlation factor equal to 86%.

The contours on the α , I_0 plane corresponding to 70% and 90% confidence level are shown in Fig. 10. The large value of the correlation factor between the estimated parameters is a result of their functional relation as indicated by Eq. (13).

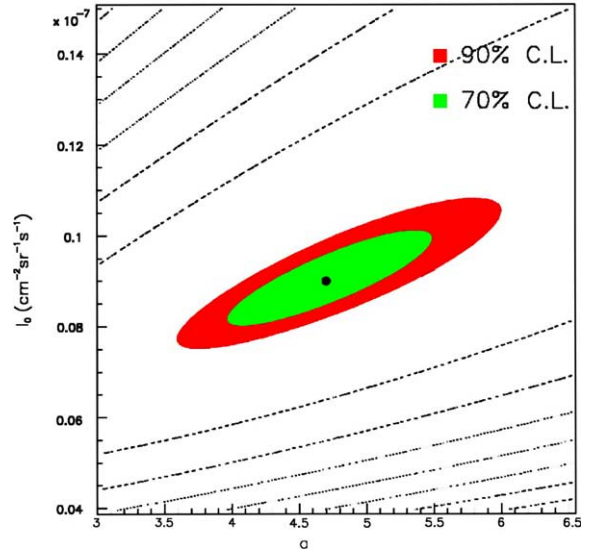


Fig. 10. The 70% and 90% confidence level limits for the simultaneous estimation of the spectral index α and the vertical muon intensity I_0 .

4. Statistical properties of the estimation technique

It is necessary to demonstrate that the analysis technique described in Section 3 does not produce any bias in the estimation of the parameters and that it correctly evaluates the error matrices. One thousand event samples have been produced,¹⁴ using the Monte Carlo simulation, with a track population corresponding to the total active experimental time at the point $\{\alpha^g = 4.8, I_0^g = 9 \times 10^{-9}\}$ ¹⁵ of the parameter space. The spectral index, $\hat{\alpha}$, the vertical intensity, \hat{I}_0 , and their error matrix, \hat{D} , were estimated by treating each test sample as a data sample.

The distribution of the estimated parametric points, $\{\hat{\alpha}, \hat{I}_0\}$, is shown in Fig. 11. The mean values and the covariant matrix of these estimations

¹³ In the fit, $b = m_i(\alpha)$ has been used, with the lower limit of the integral set to zero. The bin size was defined such that the least populated bin corresponds to a value of σ that is much less than the $0.3 \cdot m_i(\alpha)$ for all corresponding values of α . Consequently the integration is extended to at least, three standard deviations around the mean value.

¹⁴ The reconstructed zenith angle distribution density function has been evaluated by re-weighting the available Monte Carlo events produced at $\alpha^g = 4.8$ according to the production model of Eq. (4). Any set of test events was selected assuming that the reconstructed zenith angle is a random variable following the above distribution.

¹⁵ The superscript “g” indicates parameters used in generating the Monte Carlo sample.

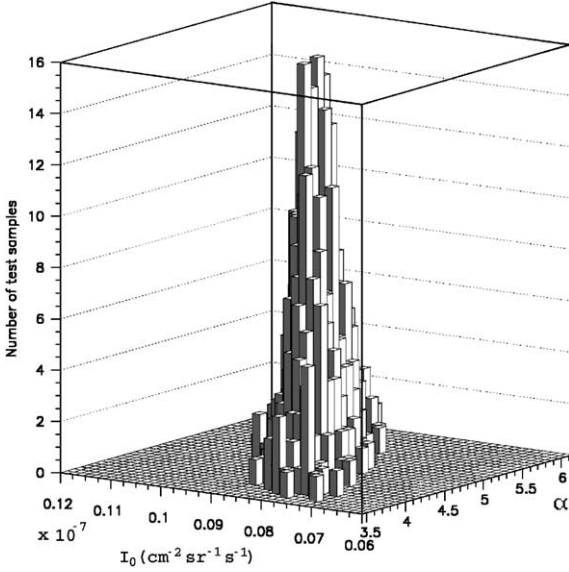


Fig. 11. A two-dimensional representation of the spectral index and vertical flux estimations using one thousand Monte Carlo test samples, produced at $\alpha^g = 4.8$, $I_0^g = 9 \times 10^{-9}$.

were evaluated by a Gaussian fit. The mean values found equal to $\langle \hat{\alpha} \rangle = 4.8$ and $\langle \hat{I}_0 \rangle = 9.0 \times 10^{-9}$, in agreement with the values of the parameters used to produce the test samples. This agreement is a demonstration that the estimations are unbiased.

Furthermore, the covariant matrix of the estimated parameters, $\{\hat{\alpha}, \hat{I}_0\}$, corresponds to $\sigma_{\hat{\alpha}} = 0.5$, $\sigma_{\hat{I}_0} = 0.7 \times 10^{-9}$ and a correlation factor of 87% which again are in a very good agreement with the estimated errors and correlation found from the data fit and shown in (14) and Fig. 10.

The absence of bias in the estimation technique is also demonstrated by the statistical properties of the quantity:

$$R = -2 \cdot \ln \frac{\mathcal{L}(\alpha^g, I_0^g)}{\mathcal{L}(\hat{\alpha}, \hat{I}_0)} \quad (15)$$

The quantity R ¹⁶ should follow a χ^2 distribution for 2 degrees of freedom [21], if the estimations are consistent. The values of the quantity R were calculated using the results of each test sample

¹⁶ The quantity R is defined as the negative of twice the logarithm of the ratio of the likelihood value at the parametric point used to generate the set of events $\{\alpha^g, I_0^g\}$ to the maximum likelihood value.

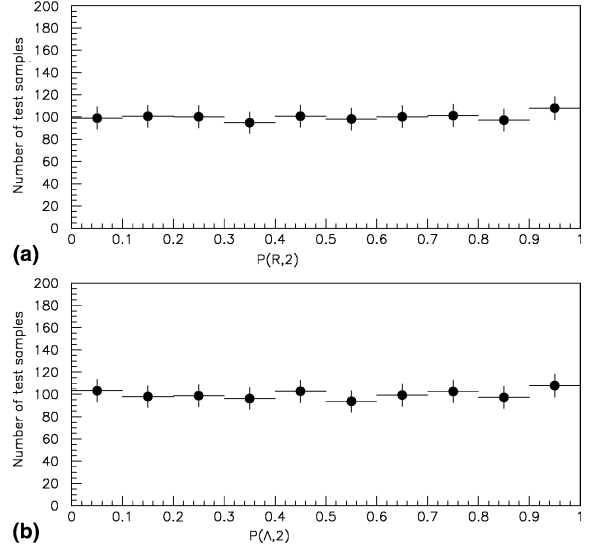


Fig. 12. (a) The χ^2 probability distribution of the quantity R (upper plot) and (b) the quantity A (lower plot), calculated using the results of each test sample fit.

fit. As shown in Fig. 12a, the χ^2 probability of the quantity R is uniformly distributed between the values 0 and 1.

The other important property of this estimation technique, the consistent evaluation of the error matrix of the estimated parameters, can be demonstrated by the distribution of the quantity, A , defined as

$$A = \begin{pmatrix} \alpha^g & -\hat{\alpha} \\ I_0^g & -\hat{I}_0 \end{pmatrix}^T \tilde{D}^{-1} \begin{pmatrix} \alpha^g & -\hat{\alpha} \\ I_0^g & -\hat{I}_0 \end{pmatrix} \quad (16)$$

With a consistent estimation of the parameter values $\{\hat{\alpha}, \hat{I}_0\}$ and the error matrix, \tilde{D} , the quantity A should follow a χ^2 distribution for 2 degrees of freedom. Fig. 12b presents the χ^2 probability distribution of the values of the quantity A evaluated for each test sample fit, demonstrating¹⁷ the consistency of the error matrix estimation.

In a further check on the simultaneous estimation of the parameters α and I_0 from the data, an iterative estimation procedure has been used that

¹⁷ The same results have been found using test samples produced at several values of the index, α , in the region between the values 4 and 5.

ignores the resolution effects.¹⁸ Re-weighted Monte Carlo events were used to calculate the differential pseudo-efficiency of the detector in reconstructing muon tracks, with respect to the zenith angle.

The pseudo-efficiency in reconstructing tracks with zenith angles in the i th bin, for a value α_0 of the index, is estimated by the ratio:

$$e_i(\alpha_0) = \frac{m_i(\alpha_0)}{m_i^o(\alpha_0)} \quad (17)$$

where $m_i(\alpha_0)$ is the number of Monte Carlo tracks that have been reconstructed and $m_i^o(\alpha_0)$ is the number of generated tracks within the i th bin.

The flux at the central value of the i th bin of the zenith angle (θ_i) is then estimated by correcting the measured zenith angle distribution as

$$\frac{dN}{d\Omega \cdot dt \cdot dS} = \frac{d_i}{2\pi \cdot e_i(\alpha_0) \cdot T \cdot \sin \theta_i \cdot \Delta\theta \cdot S} \quad (18)$$

where $\Delta\theta$ is the size of the zenith angle bin and other symbols are as defined earlier.

These corrections can only be applied to events with reconstructed zenith angles less than 90° and other tracks are ignored. A χ^2 fit to the corrected data (in equal size bins) using Eq. (4), with I_0 and α as free parameters, results to an estimation $\hat{\alpha} = \alpha_1$, which can be different from the value of the index, α_0 , used to calculate the efficiencies. In the next step, the efficiencies are calculated for a value of the spectral index equal to the estimated value and the procedure is considered to have converged when the estimations remain unchanged in two consecutive iterations.

Applying the Blind Fit to the data sample results in the following estimation:

$$\begin{aligned} \alpha &= 4.6 \pm 0.4 \\ I_0 &= 8.8 \times 10^{-9} \pm 0.6 \times 10^{-9} \text{ cm}^{-2} \cdot \text{s}^{-1} \cdot \text{sr}^{-1} \end{aligned} \quad (19)$$

which is in good agreement with the results of the re-weighting technique.

However, this method treats “blindly” the resolution effects and ignores arbitrarily the badly fitted tracks that result from an underestimation of the error.

5. Systematic errors

Systematic errors in the evaluation of the index α and the vertical intensity I_0 could be produced by the application of the selection criteria to the reconstructed tracks. Other systematic effects can come from the re-weighting of the Monte Carlo events used in the fit and from the assumptions concerning the energy dependence of the atmospheric muon flux. In addition the functional form of the parameterization of the zenith angle distribution used in the fit could add systematic bias.

It has been shown [15] that the Monte Carlo simulation of the detector describes very well the detector response. Furthermore in Section 2 it has been shown that the Monte Carlo predictions agree well with the measured distributions of the physical quantities used for the reconstruction and selection of the muon tracks. However, small differences between the data and the Monte Carlo sets, as well as correlations between the relevant physical quantities, could result in systematic effects in the estimation of the parameters. In order to quantify the magnitude of these systematic errors, the values used to define the reconstruction and track selection criteria¹⁹ have been varied. The estimation of the parameters was found to depend slightly on these selection criteria. From these variations, the systematic errors in the index, α , and vertical flux estimation are both calculated to be at the level of 2%.

In Section 4, it has been demonstrated that the re-weighting technique evaluates the muon flux parameters without any bias. However the validity of this technique is conditional on sufficient numbers Monte Carlo events in each part of the relevant phase space.²⁰ To check for possible systematic bias, tracks with reconstructed zenith angles greater than 70° were excluded from the fit. The results thus obtained remain consistent

¹⁹ Total photoelectrons per track, impact parameter and photon-likelihood value.

²⁰ If there are not enough Monte Carlo events generated at the margins of the phase space (e.g. at zenith angles around 90° , close to the horizon) the re-weighting does not describe accurately the production of muon tracks for small values of the exponent, α .

¹⁸ This is referred to as the “Blind Fit”.

with the estimations shown in (14), showing that there is no significant systematic error due to the re-weighting.

The choice of bin size when sorting the raw data of the zenith angle distribution into equal size bins, could produce systematic effects. Using the Monte Carlo events, fits have been made with several different bin sizes and the results are practically unchanged.

The zenith angle distribution of the atmospheric muons depends²¹ on the muon energy (E) at the detector depth, especially at low energies. The re-weighting of the Monte Carlo events, according to the energy integrated flux of the form of Eq. (4), conserves this dependence. As expected, the re-weighted Monte Carlo tracks, with weights as in Eq. (9) and $\alpha = 4.7$, exhibit an energy integrated distribution of the form of $\frac{dN}{d\Omega \cdot dt \cdot dS} = I_0 \cdot \cos^{4.7}(\theta)$ but the angular distribution depends on the muon energy as $\frac{dN}{dE \cdot d\Omega \cdot dt \cdot dS} = R(E) \cdot \cos^{a(E)}(\theta)$ where $a(E)$ varies from 5.3, for energies below 30 GeV, to less than 4.0 for energies greater than 2 TeV.

In the absence of experimental information on the energy of the muon, an upper limit to the systematic error due to the energy dependence of the zenith angle distribution was estimated by comparing the results found in (14) to the results of a fit to the data using a production model without any energy and zenith angle correlation.

Let

$$\frac{dN}{dE \cdot d\Omega \cdot dt \cdot dS} = \Phi(E, \theta) \quad (20)$$

be the differential atmospheric muon flux used to generate the Monte Carlo track sample. Then $\frac{dN'}{dE \cdot d\theta} = 2\pi \cdot T \cdot S \cdot \sin(\theta) \cdot \Phi(E, \theta)$.

Taking a different model that describes the atmospheric muon flux at the detector depth, according to the following equation:

$$\frac{dN'}{dE \cdot d\Omega \cdot dt \cdot dS} = C(E) \cdot \cos^\gamma(\theta) \quad (21)$$

then $\frac{dN'}{dE \cdot d\theta} = 2\pi \cdot T \cdot S \cdot \sin(\theta) \cdot C(E) \cdot \cos^\gamma(\theta)$ and the vertical intensity is given by

$$I_0 = \int_{E_{\min}}^{E_{\max}} C(E) dE$$

This model (21) does not correlate the zenith angle to the energy distribution.

The energy dependent part of Eq. (21) is chosen to be equal of

$$C(E) = \int_0^{\pi/2} \Phi(E, \theta) \cdot \sin(\theta) d\theta \quad (22)$$

In order to distribute the available Monte Carlo sample, produced by the model (20), according to the model of Eq. (21) the contribution of each muon must be weighted by the following function of energy and zenith angle:

$$\begin{aligned} w(E, \theta; \gamma) &= \frac{\frac{dN'}{dE \cdot d\theta}}{\int_{E_{\min}}^{E_{\max}} \int_0^{\pi/2} \frac{dN'}{dE \cdot d\theta} dE d\theta} \\ &= \frac{\frac{dN'}{dE \cdot d\theta}}{\int_{E_{\min}}^{E_{\max}} \int_0^{\pi/2} \frac{dN}{dE \cdot d\theta} dE d\theta} \\ &= \frac{\cos^\gamma(\theta) \cdot (\gamma + 1)}{\Phi(E, \theta)} \\ &= \frac{\cos^\gamma(\theta) \cdot (\gamma + 1)}{\int_0^{\pi/2} \Phi(E, \theta) \cdot \sin(\theta) d\theta} \end{aligned} \quad (23)$$

Using Eq. (23) to weigh the available Monte Carlo muons, the maximum likelihood fit to the data results is: $\alpha = 4.9 \pm 0.5$ and $I_0 = 9.3 \times 10^{-9} \pm 0.7 \times 10^{-9} \text{ cm}^{-2} \text{ s}^{-1} \text{ sr}^{-1}$ (with a correlation factor of 85%). The deviations from the results shown in (14) were taken as the absolute magnitudes of symmetric systematic errors due to the zenith angle and muon energy correlation.

Finally, in order to evaluate possible systematic errors due to the functional form used to express the zenith angle distribution, the energy integrated atmospheric muon flux has been parameterized as

$$\frac{dN}{d\Omega \cdot dt \cdot dS} = J_0 \cdot e^{-\frac{\beta}{\cos\theta}} \quad (24)$$

where $I_0 = J_0 \cdot e^{-\beta}$ represents the vertical intensity. The parameters I_0 and β were estimated from the

²¹ It has been found that the differential atmospheric muon flux, according to the model of [18], can be approximated to $\frac{dN}{dE \cdot d\Omega \cdot dt \cdot dS} = F(E) \cdot e^{-\frac{g(E)}{\cos\theta}}$. The exponent $g(E)$ varies from 3.4 at energies below 30 GeV up to 2.5 for energies greater than 2 TeV.

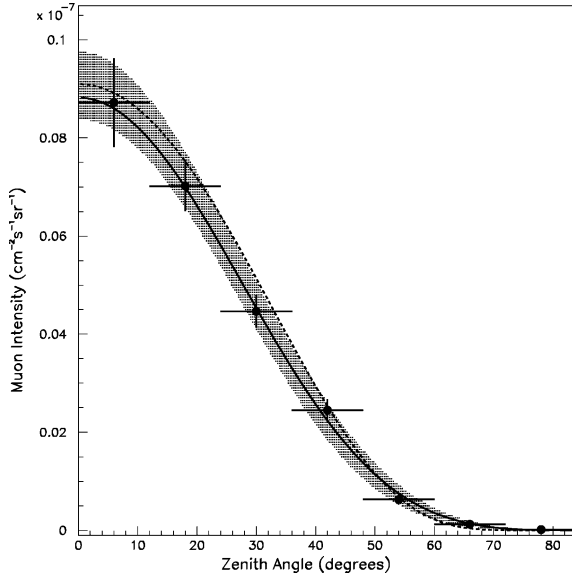


Fig. 13. Comparison of the measured atmospheric muon fluxes with results of the fits. The solid points represent data corrected for (pseudo)efficiencies in reconstructing tracks, as evaluated by the Blind Fit (19). The gray band represents the results of the fit (14) within one sigma, the solid line represents the results of the Blind Fit (19) and the dotted curve represents the solution (27) using the parameterization of Eq. (24).

data by minimizing the negative logarithm of the following likelihood function:

$$L = \prod_{i=1}^k \left[\int_{m_i(\beta)-b}^{m_i(\beta)+b} \frac{(\lambda \cdot x)^{d_i} \cdot e^{-\lambda x}}{d_i!} \times \frac{1}{\sqrt{2\pi}\sigma_i} \cdot e^{-\frac{(m_i(\beta)-x)^2}{2\sigma_i^2}} \cdot dx \right] \quad (25)$$

$$\lambda = 2\pi \cdot T \cdot S \cdot \frac{I_0 e^{+\beta} \int_0^{\pi/2} e^{-\frac{\beta}{\cos\theta}} \cdot \sin\theta \cdot d\theta}{M_0(\beta)}$$

Naturally, the bin populations $m_i(\beta)$ were evaluated as the sum of the weights:

$$w(\theta; \beta) = e^{-\frac{\beta-3.0}{\cos\theta}} \cdot \frac{\int_0^{\pi/2} e^{-\frac{3.0}{\cos\theta}} \sin\theta d\theta}{\int_0^{\pi/2} e^{-\frac{\beta}{\cos\theta}} \sin\theta d\theta} \quad (26)$$

The results of this fit

$$\beta = 3.7 \pm 0.5$$

$$I_0 = 9.1 \times 10^{-9} \pm 0.9 \times 10^{-9} \text{ cm}^{-2} \text{ s}^{-1} \text{ sr}^{-1} \quad (27)$$

correspond to an estimation of the vertical intensity, I_0 , which is in very good agreement²² with the results (14), using the parameterization of Eq. (4). The resulting distribution shape expressed by Eq. (24), for $\beta = 3.7$, agrees, within the statistical errors, with the differential flux defined by the results (14) as demonstrated in Fig. 13.

6. Results and comparisons

The results of the fit (14) have been shown to be free of statistical bias and to include a correctly estimated statistical error. The total systematic errors are evaluated as the quadratic sums of the contributions of the errors due to the track reconstruction, selection criteria and the energy dependence of the reconstruction efficiency. The reweighting, the bin size definition and the functional parameterization of the zenith angle distribution do not produce measurable systematic effects.

The final results on the spectral index and the vertical atmospheric muon intensity can be quoted as follows:

$$\alpha = 4.7 \pm 0.5(\text{stat}) \pm 0.2(\text{syst})$$

$$I_0 = 9.0 \times 10^{-9} \pm 0.7 \times 10^{-9}(\text{stat}) \pm 0.4 \times 10^{-9}(\text{syst}) \text{ cm}^{-2} \text{ s}^{-1} \text{ sr}^{-1} \quad (28)$$

with an 86% of statistical correlation between the two estimated values.

These results are consistent with other measurements of the atmospheric muon flux at similar depths; *it should be noted also that shallow experiments obtain this curve by looking at slant angles.* Previous measurements [22], found the vertical intensity of atmospheric muons to be $I_0 = 9.8 \times 10^{-9} \pm 4.0 \times 10^{-9} \text{ cm}^{-2} \text{ s}^{-1} \text{ sr}^{-1}$ at depths between 3700 and 3900 m.w.e. The exponent in the angular distribution was found to be $\alpha = 4.5 \pm 0.8$ at a depth of 3697 m.w.e. [23,24]. The DUMAND collaboration measured [25] $I_0 = 1.31 \times 10^{-8} \pm 0.4 \times$

²² The small deviation, of 1%, in the vertical muon intensity estimation from the corresponding value of (14) is much smaller than the increase in the statistical error. The agreement between the estimated value of β and the corresponding parameter of the Okada parameterization [18] of Eq. (8) should also be noted.

$10^{-8} \text{ cm}^{-2} \text{ s}^{-1} \text{ sr}^{-1}$ at a depth of 3707 m.w.e. and $\alpha = 6_{-1}^{+7}$ for 4157 m.w.e.

There is also good agreement between the present measurement of the vertical atmospheric muon intensity and existing phenomenological model parameterizations. The Okada model [18] predicts a vertical flux of $8.8 \times 10^{-9} \text{ cm}^{-2} \text{ s}^{-1} \text{ sr}^{-1}$, whilst the model of Bugaev et al. [1,2] predicts, $I_0 = 9 \times 10^{-9} \text{ cm}^{-2} \text{ s}^{-1} \text{ sr}^{-1}$ (see also [3]) for a depth of 3800 m.w.e.

The predicted shape of the zenith angle distribution by the Okada model [18] is found to be in agreement with these measurements [15]. Furthermore, using the parameterization of Eq. (24), the exponent β has been estimated to be 3.7 ± 0.5 whilst the Okada parameterization of the energy integrated flux corresponds to a value of β equal to 3.0.

7. Conclusions

Atmospheric muons have been detected and their trajectories reconstructed using a test element of the NESTOR detector deployed in a depth of 3800 m at the experimental site and connected to the shore laboratory by a 30 km long electro-optical cable. The basic detection and reconstruction techniques, developed by the NESTOR collaboration, have been extensively tested and shown to be satisfactory.

Despite the limited size of this test detector array, the vertical intensity and the zenith angle distribution of cosmic ray muons at the detector depth have been measured and found to be consistent with previous underwater measurements and with phenomenological predictions.

The measured vertical muon intensity and the index α , at a depth of 3800 m.w.e., are

$$\alpha = 4.7 \pm 0.5(\text{stat}) \pm 0.2(\text{syst})$$

$$I_0 = 9.0 \times 10^{-9} \pm 0.7 \times 10^{-9}(\text{stat}) \\ \pm 0.4 \times 10^{-9}(\text{syst}) \text{ cm}^{-2} \text{ s}^{-1} \text{ sr}^{-1}.$$

Acknowledgements

The authors wish to acknowledge the help and support of all the members of the NESTOR

collaboration. Our very sincere thanks are also due to the technical and support staff from the collaborating institutes, especially of the NESTOR Institute in Pylos and the “Institut für Angewandte Physik”, University of Kiel, for their unstinting efforts over several years. It is also a pleasure to acknowledge our many industrial partners for their essential contributions; in particular we express our gratitude to OTE S.A, the Greek Telecom Company for the substantial material support and for the sea and underwater operations that underpin the results presented here. Many thanks are due to the Masters, Crews and Cable Engineers on the THALES (OTE) and RAYMOND CROZE (France Telecom marine) and TENEO (Tyco) as well as the support vessel DYNATOS, for their help and advice in sea operations and deployments.

Last but not least, we greatly appreciate the support of many institutes and agencies that have provided funding for the NESTOR project; in particular the General Secretariat for Research and Technology of the Greek Ministry of Development, the General Secretariat of Peloponnesus and the German Bundesministerium für Bildung und Forschung, Germany. We are also grateful to the Wolfermann-Naegeli foundation in Kuesnacht (CH) for its support in the preparation phase leading to the results discussed in this paper. We hope that the completion of this important stage in this project demonstrates that their confidence was not misplaced.

References

- [1] E.V. Bugaev et al., in: L.K. Resvanis (Ed.), Proceedings of the 3rd NESTOR International Workshop, 1993, p. 268.
- [2] E.V. Bugaev et al., *Physics Review D* 58 (1998) 054001.
- [3] P.K.F. Grieder, *Cosmic Rays at Earth*, Elsevier, Amsterdam, 2001 (Chapter 3).
- [4] P. Le Coultre, The L3+Cosmics experiment, *Nuclear Physics B (Proc. Suppl.)* 122 (2003) 161–169.
- [5] O. Adriani et al., *Nuclear Instruments and Methods in Physics Research A* 488 (2002) 209–225.
- [6] Pylos, in: L.K. Resvanis (Ed.), Proceedings of the 2nd NESTOR International Workshop, 1992.
- [7] Pylos, in: L.K. Resvanis (Ed.), Proceedings of the 3rd NESTOR International Workshop, 1993.
- [8] E.G. Anagnostis et al., *Nuclear Instruments and Methods A* 479 (2002) 439–455.

- [9] S.A. Khanaev, A.F. Kuleshov, in: L.K. Resvanis (Ed.), Proceedings of the 2nd NESTOR International Workshop, 1992, p. 253.
- [10] E.G. Anassontzis et al., Nuclear Instruments and Methods A 349 (1994) 242–246.
- [11] E. Trimonis, M. Rudenko, in: L.K. Resvanis (Ed.), Proceedings of the 2nd NESTOR International Workshop, 1992, p. 321.
- [12] T.A. Demidova, I.A. Repin, in: L.K. Resvanis (Ed.), Proceedings of the 2nd NESTOR International Workshop, 1992, p. 284.
- [13] L.K. Resvanis, Proceedings of the 8th International Workshop on Topics in Astroparticle and Underground Physics (TAUP), 2003.
- [14] P.K.F. Grieder, Proceedings of the 28th International Cosmic Ray Conference (ICRC), 2003.
- [15] G. Aggouras et al., Operation and performance of a NESTOR test detector, Nuclear Instruments and Methods A (2005), submitted for publication.
- [16] D. Nygren et al., NESTOR Data Acquisition System—Based on Waveform Capture, LBNL, August 20, 1998.
- [17] P. Arragain, NESTOR DAQ System on Shore, LBNL, October 1999.
- [18] A. Okada, Astroparticle Physics 2 (1994) 393.
- [19] G.K. Fanourakis et al., Nuclear Instruments and Methods A 412 (1998) 465–474.
- [20] F. James, M. Roos, ‘MINUIT’ a system for function minimization and analysis of the parameter errors and correlations, Computer Physics Communications 10 (1975) 343–367.
- [21] Eadie et al., Statistical Methods in Experimental Physics, Elsevier, Amsterdam, 1988.
- [22] I.F. Barinov et al., in: L.K. Resvanis (Ed.), Proceedings of the 2nd NESTOR International Workshop, 1992, p. 340.
- [23] L.K. Resvanis (Ed.), Proceedings of the 2nd NESTOR International Workshop, 1992, pp. 1–19.
- [24] L.K. Resvanis et al., NESTOR: a neutrino particle astrophysics underwater laboratory for the Mediterranean, in: V.J. Stenger, J.G. Learned, S. Paksava, X. Tata (Eds.), Proceedings of the High Energy Neutrino Astrophysics Workshop, Hawaii, 1992.
- [25] J. Babson et al., Physical Review D 42 (1990) 3613.